

CrossMark
click for updatesCite this: *J. Mater. Chem. A*, 2015, 3,
17135Received 3rd April 2015
Accepted 23rd July 2015

DOI: 10.1039/c5ta02416a

www.rsc.org/MaterialsA

Fast mass interdiffusion in ceria/alumina composite

F. Teocoli,^a D. W. Ni,^a S. Sanna,^a K. Thydén,^a F. C. Fonseca^b and V. Esposito^{*a}

Gadolinium-doped ceria (CGO) presents unique processes at low oxygen partial pressure ($pO_2 < 10^{-12}$ atm) and low temperatures ($T > 800$ °C) such as faster mass diffusion, which are not observed in conventional sintering under ambient air conditions. In CGO/ Al_2O_3 composites the resulting effects driven by such mass diffusion are low viscosity flows and high reactivity between phases, indicated by the formation of $CeAlO_3$. This reaction is promoted by the high content of oxygen defects and the chemical reduction of Ce^{4+} cations to Ce^{3+} in CGO/ Al_2O_3 composites under low temperature and low pO_2 . In this work, a comparison is made between sintering CGO/ Al_2O_3 under ambient air conditions and under low pO_2 , focusing on densification, viscosity and the evolution of the microstructure.

1. Introduction

Cerium oxide based compounds are key-materials in several cutting-edge technologies. Traditionally associated to catalysis, environmental and various energy applications,^{1–5} their importance is mainly due to the unique combination of properties such as high ionic conductivity (*i.e.* oxygen vacancies concentration and mobility) along with mixed electronic and ionic conductivity, large oxygen storage and exchange capabilities.^{1–6} These properties are also supplemented by an exceptionally high chemical resilience against reactive gases (*e.g.* SO_x , NO_x , CO, CO_2 , hydrocarbons *etc.*), solids and many other reactive compounds.^{7–10} Therefore, ceria-based materials (*e.g.* lanthanides doped ceria such as Sm-, Gd-, and Nd-doped $CeO_{2-\delta}$) are gaining significant importance in a wide range of novel applications that require chemical stability under harsh conditions. Emerging technologies such as catalytic supports in solar-driven thermochemical H_2O/CO_2 splitting and chemical looping, are based on the distinctive properties of ceria.^{4,11} The chemical and the microstructural stability of ceria is crucial considering the harsh conditions it is expected to withstand such as chemical cycling in oxidative (high pO_2) and reducing environments (low pO_2) at high temperatures (800–1500 °C).^{12,13}

Although ceria compounds are usually considered very stable materials there are some important exceptions. In our previous work, we showed that aliovalent doped ceria (*i.e.* Gd-doped ceria) can actually undergo fast mass diffusion processes at low oxygen partial pressure ($pO_2 < 10^{-12}$ atm) above 800 °C. This can lead to severe microstructural transformations.^{14–17} The fast mass diffusion promotes a rapid grain

growth, resulting in coarsening of nanometric grains up to several microns in a few minutes, at relatively low temperature (900–1100 °C).¹⁴ Furthermore, the same process leads to high densification of the compacted powders of various morphologies with very little residual porosity.^{14,15} The same remarkable effects are observed in highly porous CGO bodies with relative density below 35 vol%, in which the natural constrain of the supercritical porosity (*i.e.* large and thermodynamical stable porosity), unexpectedly cannot prevent a full densification of the material.¹⁵

A mechanistic explanation by a quantitative analysis of fast mass diffusion effects was given based on the peculiar chemistry of CeO_2 .^{14,18} The chemical reduction of cerium oxide from Ce^{4+} to Ce^{3+} , as well as the related change in oxygen vacancy concentration, plays a significant role on such mass diffusion processes.¹⁸ In the presence of oxygen gas (*e.g.* in air, in the oxidized state Ce^{4+}) mass diffusion is greatly inhibited and the material is generally stable.^{18,19} On the other hand, in the presence of reactive gases which can reduce Ce^{4+} to Ce^{3+} and produce oxygen vacancies, significant transformation in the microstructure and thermo-mechanical properties are driven by mass diffusion at relatively low temperatures (*e.g.* at $T > 800$ °C).

Due to its importance in several technological areas which doped-ceria is either processed or operates in both reducing and oxidative conditions at high temperatures,¹² a deeper understanding of the consequences of such fast mass diffusion mechanisms is crucial. Particularly in this study we investigate diffusion effects in ceria-based mixed-metal oxides composites, having Al_2O_3 as the selected secondary phase. Composites materials have generally different mass diffusion mechanisms with respect to their individual phases,²⁰ and CeO_2/Al_2O_3 systems have especially high relevance in several catalytic and electrochemical applications.^{21–24} Alumina has usually very limited solubility in CeO_2 ,²⁵ thus nanometric alumina is added in the ceria matrix as secondary phase. A fine solid dispersion of alumina can limit mass diffusion processes in ceria, *e.g.* by

^aDepartment of Energy Conversion and Storage, Technical University of Denmark (DTU), Frederiksborgvej 399, DK-4000 Roskilde, Denmark. E-mail: vies@dtu.dk; Tel: +45 4677 5637

^bNuclear and Energy Research Institute – (IPEN-CNEN/SP), 05508-000, São Paulo, SP, Brazil

pinning the grain boundary during sintering at high temperatures by the so-called Zener's pinning effect.²⁶ In this study we focus on the combined effects of chemical reduction and temperature on mass diffusion processes in ceria–alumina systems. Such diffusive processes have activated viscous mass flow and solid state reactions that significantly changed the relative density and microstructure (grain growth and porosity), which in turn, affected the overall composition and electrochemical properties of the composite.

2. Experimental section

2.1. Materials and sample preparation

Commercial $\text{Ce}_{0.9}\text{Gd}_{0.1}\text{O}_{1.95-\delta}$ powder ("ultra-low surface area" CGO powder by Rhodia, France) with specific surface area of $6.5 \text{ m}^2 \text{ g}^{-1}$, and primary particle size around 130 nm, and nanometric $\alpha\text{-Al}_2\text{O}_3$ powder (aluminum oxide by Alfa Aesar GmbH & Co KG, Germany) with specific surface area of $180 \text{ m}^2 \text{ g}^{-1}$, and primary particle size around 40–80 nm, were mechanically mixed in a roller miller to fabricate CGO/ Al_2O_3 composite with 10 vol% of alumina. A 50 vol% pellet was prepared and treated in reducing conditions for the XRD characterization. For pellets preparation, 3 wt% aqueous polyvinyl-acetate (PVA) binder was added to the powder ($\sim 0.05 \text{ ml g}^{-1}$). Uniaxial pressing at 170 MPa for 30 s was used to prepare cylindrical samples of CGO/ Al_2O_3 with 8 mm diameter and rectangular bars ($15 \text{ mm} \times 5 \text{ mm}$), both with 1 mm thickness. Green density of both types of CGO/ Al_2O_3 samples was around 40%.

2.2. Thermomechanical analysis

Thermo-mechanical analysis (TMA 402 F1 Hyperion, Netzsch, Germany) was used for dilatometry and viscoelastic characterization. The dilatometry was carried out on cylindrical samples both in air and in reducing conditions.^{15–17} All samples were fired continuously in air at a heating rate of $0.33 \text{ }^\circ\text{C min}^{-1}$ from room temperature to $400 \text{ }^\circ\text{C}$ and held for 4 hours to ensure complete removal of organic compounds. After eliminating the binder, the samples were sintered at a heating rate of $1 \text{ }^\circ\text{C min}^{-1}$ to $1450 \text{ }^\circ\text{C}$ and kept for 1 hour at $1450 \text{ }^\circ\text{C}$. Sintering, from $400 \text{ }^\circ\text{C}$ to $1450 \text{ }^\circ\text{C}$, was performed in air ($p\text{O}_2 = 0.21 \text{ atm}$) or in dry gas mixture 9% $\text{H}_2/91\% \text{ N}_2$ ($10^{-31} < p\text{O}_2 < 10^{-12} \text{ atm}$, depending on temperature)¹⁴ flowing at 60 ml min^{-1} . The uniaxial viscosity of samples was measured by thermo-mechanical analyzer performing cyclic loading dilatometry on rectangular bars, as reported in ref. 15 and 16. For the viscoelastic characterization, both in air and under reducing conditions, the same sintering profile of dilatometric measurements was used. It is important to highlight the fact that the composite samples treated in reducing conditions were cooled down in controlled re-oxidative conditions at $900 \text{ }^\circ\text{C}$ as reported in ref. 17. This method thoroughly re-oxidizes the materials and avoids mechanical shocks to the samples, which may lead to formation of cracks and eventual mechanical failures, usually associated with the chemical expansion–contraction process in the elastic regime at low temperatures.^{14–17}

2.3. Microstructure, chemical and phase analysis

The microstructure of samples sintered both in air and under reduced oxygen partial pressure was observed using scanning electron microscopy (SEM) using a Carl Zeiss field emission microscope (SUPRA 35 and Zeiss CrossBeam 1540XB) for high resolution imaging of mechanically polished and cold fractured cross sections. The micrographs were used to compare the final microstructure of the samples sintered in different $p\text{O}_2$ in order to investigate the effect of the holding time at the sintering temperature and the limited activity registered during cooling.¹⁷ The relative densities of the samples after sintering were estimated by SEM image analysis using freeware software ImageJ®.

Energy selective backscattered detector (EsB, Cross Beam 1540XB) was used to define microstructural and compositional features of samples. Elemental analysis was carried out to determine the stoichiometry of the materials after the thermochemical treatments by using energy-dispersive X-ray spectroscopy (EDX) with a Thermo Electron Corporation detector.

Phase characterization of the samples was performed by X-ray diffraction (XRD) in Bragg–Brentano θ – 2θ scans configuration using a Rigaku RU-200 rotating Cu anode as source, operating at 50 kV, 200 mA, over a 20 – 85° angular range, with step size of 0.02° and 2 s acquisition time at each step. The X-ray beam point-source was monochromatized and collimated ($\lambda = 1.5418 \text{ \AA}$) by a multilayer optic.

2.4. Electrochemical characterization

Electrochemical impedance spectroscopy (EIS) measurements were performed with a frequency response analyser (Solartron 1260, UK) in the temperature range 200 – $750 \text{ }^\circ\text{C}$ in static air. Samples used for EIS measurements were polished to a uniform size, typically 7 mm diameter and 1 mm thick. Before EIS data collection samples were held for $\sim 30 \text{ min}$ at each measuring temperature to allow thermal equilibration. EIS analysis was carried out in the frequency range of 10^7 to 1 Hz with 100 mV ac voltage amplitude and zero dc bias. High-purity platinum paste, cured at $800 \text{ }^\circ\text{C}$, was used to prepare the electrodes in Pt/CGO– Al_2O_3 /Pt symmetric cell configuration. The EIS sample holder, with platinum leads and type K thermocouple positioned close to three samples, measured at same temperature, was inserted in an alumina tube placed in a resistive tube furnace.²⁷ The electrical conductivity was determined by fitting EIS diagrams normalized by the geometric factor of samples. The EIS diagrams measured at low temperatures ($T < 400 \text{ }^\circ\text{C}$) were fit to an equivalent circuit composed of two parallel resistor/constant phase element (CPE), connected in series.²⁸ At higher measuring temperatures EIS diagrams were fitted to a single resistor. Thus, both blocking and bulk resistance were resolved at low temperatures ($T < 400 \text{ }^\circ\text{C}$), whereas at higher measuring temperature only the total resistance (bulk + blocking) was obtained from EIS data.

3. Results and discussion

3.1. Mass diffusion phenomena

According to the mass conservation law and the electro-neutrality principle, mass diffusion in ionic materials is driven

by a simultaneous rearrangement of both negative and positive ions in the crystalline lattice. Such laws govern diffusion processes that control sintering of particles, porosity annihilation (*i.e.* densification), grain growth, recrystallization, *etc.*²⁶ In metal oxide, cation diffusion is generally the limiting step for mass diffusion. Particularly in fast ionic conductors such as doped-CeO_{2-δ}, oxygen defects are highly mobile and abundant in the lattice. This feature gives a typical oxygen self-diffusion coefficient that is more than 9 orders of magnitude higher than that of cations.²⁶ Ceria presents peculiar diffusive properties associated with solute drag controlled phenomena.¹⁸ The solute drag in ceria is related to the fact that aliovalent cations such as impurities, dopants and cerium itself as Ce³⁺, can have different sizes and valences with respect to the hosting cation (Ce⁴⁺). Such differences induce a “trap effect” for cation diffusion.¹⁸

Recent studies have reported that highly defective doped-ceria under low oxygen partial pressure ($pO_2 < 10^{-12}$ atm) exhibits enhanced diffusion of cations through the lattice that is activated at low temperatures by the reduction of Ce⁴⁺ to Ce³⁺.¹⁴ This process is the result of a combined effect of a change in the cation size (Ce⁴⁺ to Ce³⁺) and electrostatic equalisation of the host cation Ce³⁺ with the dopant (Gd³⁺). Evidences of such enhanced mass diffusion are especially registered as a fast grain growth and densification.¹⁴ A nearly full densification occurs at temperatures below 1200 °C, even starting from low green density bodies or coarse primary particles.^{14–17} Grain boundary mobility in CGO, which is directly proportional to the diffusion coefficient of the limiting species (solute cations), changes by several orders of magnitude, *e.g.* increasing from $\sim 10^{-16}$ m³ N⁻¹ s⁻¹ to $\sim 10^{-7}$ m³ N⁻¹ s⁻¹ at 1400 °C, which correspond to net diffusion coefficients of 10^{-19} cm² s⁻¹ and 10^{-10} cm² s⁻¹, respectively.¹⁸ A substantial change in the viscoelastic behaviour of the material during sintering under reducing conditions has been observed as additional evidence. Particularly in reducing conditions, a decay of viscosity to 20–40 GPa s due to the mass flow is observed at temperatures lower (900 °C) than that in oxidative conditions (1200 °C).^{16,17}

Sintering behaviour and viscoelastic characterization have been thoroughly investigated by dynamic thermal-mechanical analysis (TMA). Such measurements allow characterising the mass diffusion-driven viscous processes that lead to densification of compacted powders, as well as the viscoelastic response of the consolidated material under mechanical stimuli during thermal processes and sintering.^{15,16,29} TMA was carried out on the CGO/Al₂O₃ composites. Fig. 1 shows the results for CGO/Al₂O₃ compacts measured in air and in 9% H₂/N₂. TMA data of CGO from a previous study, taken in the same conditions, are also displayed for comparison.¹⁶ Fig. 1a shows the densification and densification rates, expressed as linear shrinkage of CGO/Al₂O₃ and CGO as a function of temperature. Due to the fast mass diffusion in reducing conditions, the onset of linear shrinkage of CGO takes place at relatively low temperatures (~ 900 °C) and the densification process completes at 1200 °C. On the other hand, the densification of the CGO/Al₂O₃ composite is limited and activated at higher temperatures than the one of CGO. Despite the lower onset

temperature for the linear shrinkage occurring in reducing condition (1100 °C with respect to 1250 °C in air), a significant lower degree of densification was obtained in 9% H₂/N₂ atmosphere than that obtained in air. The calculated relative densities in 9% H₂/N₂ and in air are 70% and 80%, respectively.

Fig. 1b shows the shrinkage rates that are the derivatives with respect of the time of the data in Fig. 1a. This plot gives an effective graphical representation of the mass diffusion rate during the densification process. The maximum shrinkage rates at $2\text{--}3 \times 10^{-5}$ s⁻¹ for CGO/Al₂O₃ sintered in different conditions is found at the same temperature ($T = 1300$ °C) regardless of the pO_2 , showing that the diffusion processes in the composite samples occur at high temperatures only. This is substantially different of the CGO sample, in which the maximum mass diffusion rate of 3×10^{-5} s⁻¹ is registered at 1100 °C. Therefore, conversely to the pure CGO, the densification of CGO/Al₂O₃ in 9% H₂/N₂ seems to be unaffected by the reduction of Ce⁴⁺ to Ce³⁺.

Nevertheless, limited densification is normally observed in ceramic composites materials.¹⁹ As for highly porous materials, slow mass diffusion in multiphase systems is usually attributed to inhibitive effects that the secondary phase can have on the diffusive paths (*i.e.* grain boundary diffusion, surface diffusion and lattice diffusion) of the primary (matrix) phase.^{26,30} Particularly, an insoluble dispersed phase such as the Al₂O₃ nanometric particles in CGO, can possibly lead to Zener's pinning effect, limiting thus the mass diffusion mechanism at the grain boundary, which is known to be the step limiting rate for sintering and densification of CGO.¹⁸

In order to obtain a comprehensive understanding of the viscous flow during the sintering, viscoelastic properties were investigated during sample consolidation. The uniaxial viscosity decreases with the mass diffusion increase during the preliminary and intermediate stages of the sintering. On the other hand, the viscosity increases back again during the grain growth and final densification of polycrystalline samples in the later stage of the sintering.^{16,29} Fig. 2 shows the uniaxial viscosities of the CGO/Al₂O₃ composite calculated as a function

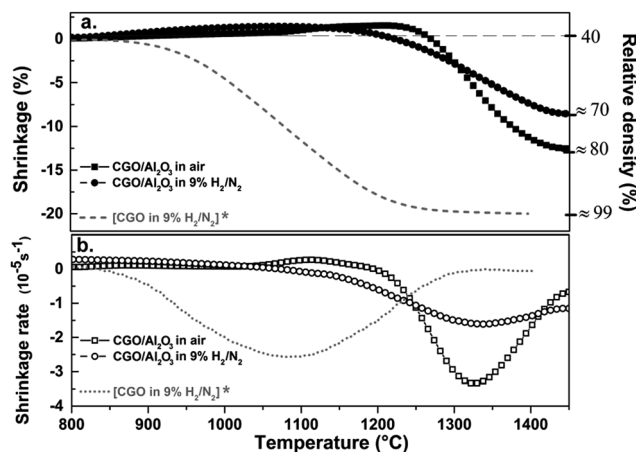


Fig. 1 (a) Densification and (b) densification rate of CGO/Al₂O₃ composites sample under air and 9% H₂/N₂ mixtures (*densification for CGO in 9% H₂/N₂ from ref. 16).

of sintering temperature both in air and under 9% H_2/N_2 . This plot also displays the viscosity calculated for pure CGO at the same thermal conditions under 9% H_2/N_2 extracted from ref. 16. In all cases the uniaxial viscosities were calculated at the onset temperatures, where the elastic-to-viscous transition appeared in the TMA (*i.e.* where the samples consolidate in a continuum body and/or are not solely elastic).²⁹ Despite the similar $p\text{O}_2$ -independent, limited sintering behaviour of the composites shown in Fig. 1, a thorough analysis of the visco-elastic behaviour by TMA reveals a remarkable effect of the atmosphere on the composite. Fig. 2 shows that in reducing conditions the viscosity decays gradually from 400 to 2.5 GPa s and at lower temperatures as compared to its air sintered counterpart. Such an effect is due to an increased mass flow taking place in the composite sample sintered in 9% H_2 . However, as discussed in Fig. 1 and differently from the CGO sample (also shown in Fig. 2), such mass flow does not correspond to a fast densification of the composite sample. Particularly, Fig. 2 shows that the minimum viscosities are found at around 1350 °C for both composite samples treated in air and in 9% H_2/N_2 . This temperature corresponds in Fig. 1b to the point of maximum sintering activity, where, however, the relative density is below 70% (Fig. 1a). Moreover, Fig. 2 shows that for temperatures above 1350 °C the viscosity of the CGO/ Al_2O_3 treated in air increases with increasing temperature towards the final steps of the densification. This behaviour is usually attributed to a microstructural change in the samples, from a porous to a dense continuum body.^{16,29} The same effect is clearly observed in Fig. 2 for CGO sample in reducing conditions, which densifies easily at low temperatures.¹⁶ On the contrary, such an effect is not observed for the composite sintered in 9% H_2/N_2 , where the viscosity values remain below 3 GPa s for $T > 1300$ °C. Considering that the composite samples sintered in different conditions exhibit similar densifications (Fig. 1), the observed differences on viscous behaviours suggest that distinct mass diffusion occur depending on the sintering atmosphere. Moreover, such a difference cannot be attributed to the density of the samples, which are comparable at any temperature, as inferred from the dilatometry in Fig. 1.

3.2. Microstructural and compositional features

Microstructural characterization of the samples after TMA gives a clear understanding concerning the effects of the diffusive process discussed in 3.1. Fig. 3 shows polished cross section SEM images for CGO/ Al_2O_3 samples treated in air (Fig. 3a) and in 9% H_2/N_2 (Fig. 3b) after sintering at 1450 °C for 1 h. The composites are porous and multi-phased. Chemical contrast at the micrograph is obtained by backscattered electrons while the chemical compositions were inferred by EDX analysis. Image analysis confirms dilatometry results, indicating that the relative density of CGO/ Al_2O_3 was 80% and 70% in air and in 9% H_2/N_2 conditions, respectively. Alumina nanoparticles morphology is detected in the CGO matrix. These nanoparticles seem to segregate in clusters of a few microns (see Fig. 3 insets). The Al_2O_3 particles remarkably maintained their nanometric features with limited signs of sintering even after the high

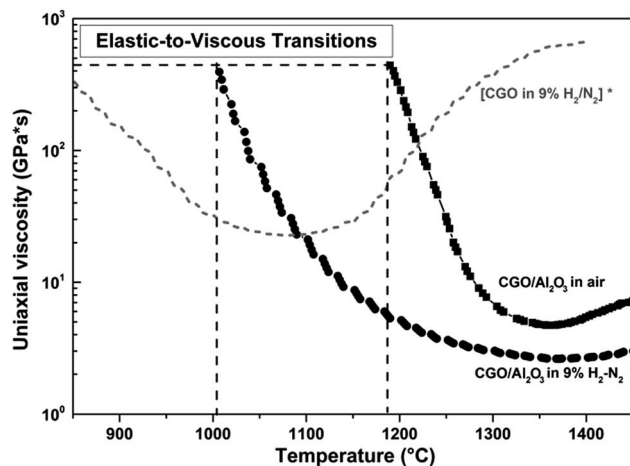


Fig. 2 Uniaxial viscosity as a function of temperature for CGO/ Al_2O_3 sintered in air and in 9% H_2/N_2 (*uniaxial viscosity for CGO in 9% H_2/N_2 from ref. 16 is also reported as reference).

temperature treatment at 1450 °C for 1 hour. Although Fig. 3 shows similar microstructures for both sintering conditions, a closer inspection at higher magnification by backscattered electrons (Fig. 3 insets) reveals important features. For the sample sintered in air (inset a), the CGO matrix appears continuous and sintered with a residual porosity mainly localized at the Al_2O_3 nanoparticles and at its interface with the CGO matrix. Conversely, for the sample treated in reducing conditions (inset b), CGO matrix is discontinuous with limited grain growth. The Al_2O_3 particles are hardly observed at the cross section and an additional porous phase, evenly distributed in the material, can be detected. This additional phase is detected due to a marked difference in contrast with the CGO matrix. The additional phase is mainly featured within porous regions of the sample with a distinctive morphology. Such unexpected phase exhibits sponge-like features and shell-like formations surrounding the remaining Al_2O_3 nanoparticle clusters. Such phase is not detected in composites sintered in air, in which the interface between the two phases is quite sharp (Fig. 3a). A closer look to the Fig. 3b inset also indicates the presence of complex microstructural and compositional features, which is a strong indication of chemical reaction between the starting components in samples treated in 9% H_2/N_2 . The observed morphology arranged in a nanocomposite with a lamellar shape suggests an intense interdiffusion. The presence of additional phases results from a solid state reaction between CGO and Al_2O_3 , a feature further confirmed by elemental analysis EDX.

Fig. 4 shows the SEM-EsB imaging and the EDX elemental map analysis of polished cross sections of samples treated in 9% H_2/N_2 . Elemental mapping indicated that the sample treated in reducing conditions form an intermediate phase based on Ce, Al, Gd and O (not shown). Quantitative EDX analysis also shows that the atomic ratio between the Ce and Al is around 50/50 in such intermediate phase. Due to the limitations on the EDX resolution, the composition associated to the fine microstructure shown in Fig. 3b inset could not be clarified. No impurities were detected by EDX. Net mass

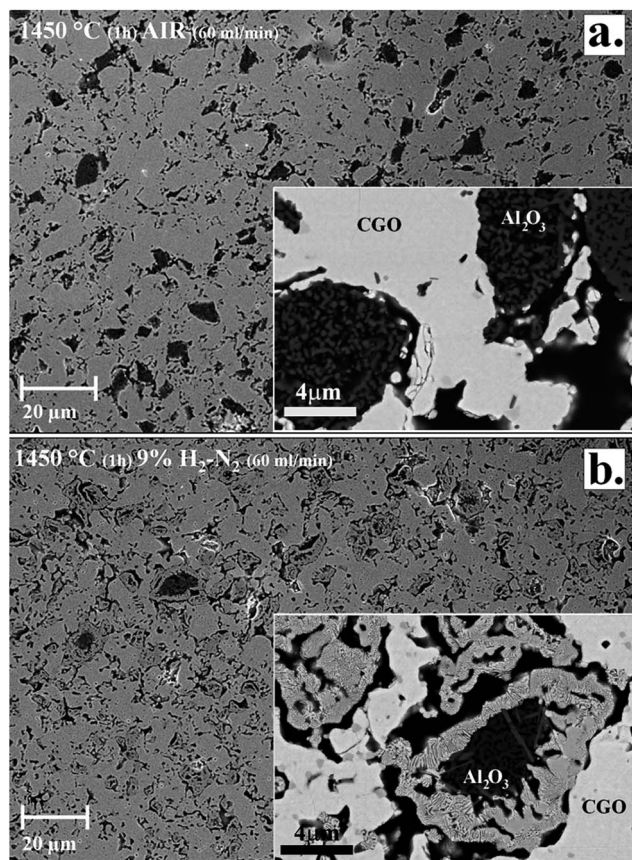


Fig. 3 SEM images of polished cross section for CGO/Al₂O₃ samples treated (a) in air and (b) in 9% H₂/N₂ after sintering at 1450 °C for 1 h. The inset images are taken with backscattered electrons giving a chemical contrast of the different phases.

diffusion in CGO/Al₂O₃ composited treated in 9% H₂/N₂ was estimated by measuring the volume of the new phase formed at the CGO–Al₂O₃ interface and by considering the maximum temperature and the time of the treatment (*i.e.* 1450 °C for 1 hour) as the main parameters in phase growth process. The images analysis was carried out on several cross section images to ensure meaningful statistics. The calculation indicates that the phase is formed at 1450 °C with a typical diffusion coefficient of 10⁻¹⁰ cm² s⁻¹. This value is remarkably similar to the one estimated for pure ceria in the same conditions and strongly suggests that the Al–Ce interdiffusion leading to the new phase is still dominated by CGO cations.^{14,18} Moreover, the fact that the CGO–Al₂O₃ interface in samples treated in air is sharp with no detected chemical reaction (see inset Fig. 3a) confirms that the elemental interdiffusion increases several order of magnitude when atmosphere changes from oxidative to reducing.

From the perspective of the solid state chemical reaction between ceria and alumina, the large amount of the additional phase, at the expense of Al₂O₃ nanoparticles, indicates that such reaction was driven by fast mass diffusion in reducing conditions, in which ceria is highly defective with oxygen vacancies and Ce³⁺ species. Conversely, the sample treated in air, with

lower concentration of both oxygen defects and Ce³⁺, no traces of interfacial diffusion were found. On the other hand, the formation of a complex microstructure in the reduced sample suggests that the precipitation of the original phases could also have taken place at the high temperature re-oxidation step (900 °C), where the equilibrium is again shifted toward the CGO and the Al₂O₃ phases.

However, the hypothesis of an intense solid state reaction between ceria and alumina is consistent with the TMA results which indicate that the composite flows viscously at low temperatures in 9% H₂/N₂ (Fig. 2). As discussed in Fig. 1 and 2, the viscous flow during sintering limits densification. Therefore, the formation of the additional phase above 1000 °C can lead to a mass flow that does not necessarily result in densification of the sample. Such hypothesis is supported by the fast mass diffusion processes in reducing conditions previously described for CGO.^{14–18} Therefore, it is reasonable to conclude that in the case of the CGO/Al₂O₃ composite, the fast mass diffusion observed with pure CGO in reducing conditions is directed towards a solid state reaction between the Al₂O₃ and CGO phases rather than densification and grain growth. From the microstructural characterisation it is also evident that the formation of such new phase can inhibit the diffusion in CGO, limiting the densification and grain growth.

3.3. Phase analysis

Fig. 5 shows XRD analysis carried after sintering at 1450 °C in air and in 9% H₂/N₂ (bottom panel). XRD data show that the CGO is the dominant phase (triangle marks) and alumina was not detected due to the low relative volume fraction (10 vol%). Nevertheless, for the sample treated in 9% H₂/N₂, additional peaks with low relative intensity were detected (circle marks). Although this is a minor component, the indexed peaks revealed unambiguously the symmetry of a ceria aluminate-based (CeAlO₃) phase. Such a result was further confirmed by XRD on samples with higher Al₂O₃ content. Fig. 5 (top panel)

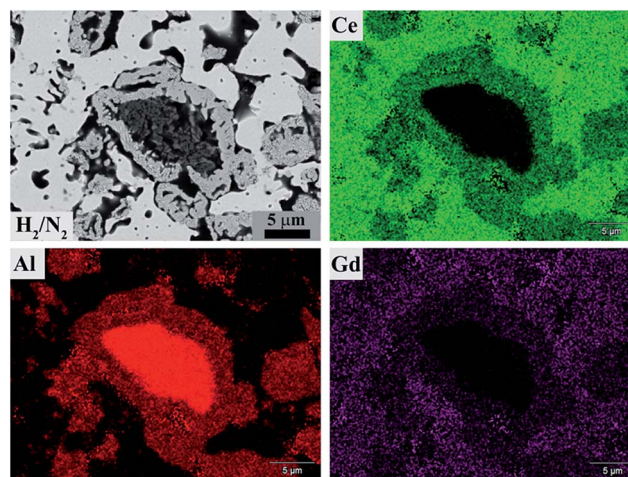
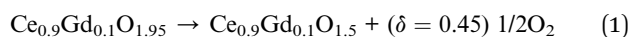


Fig. 4 SEM images and corresponding EDX elemental mapping of CGO/Al₂O₃ samples (10 vol% Al₂O₃) treated in 9% H₂/N₂ at 1450 °C for 1 hour (polished cross section).

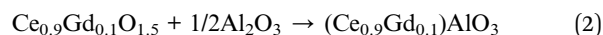
shows the XRD pattern for a sample with 50 vol% Al_2O_3 treated in the same conditions (sintering in reducing atmosphere followed by high temperature re-oxidation). Experimental data clearly showed the presence of CeAlO_3 along with unreacted (or segregated) alumina and CGO. It is worth mentioning that CeAlO_3 is usually very difficult to be synthesized by solid state reaction. Such a phase has been synthesized by wet chemical and combustion methods,^{31,32} and by solid state reactions at high temperature (1500–1600 °C) within inert gases and vacuum environments.³³ On the other hand, formation of CeAlO_3 in traces at the surface of Ni/ CeO_2 - Al_2O_3 catalytic systems has been detected in the catalytic reforming of methane at around 800 °C.²³ Such result is consistent with our findings, which indicated that reducing condition is required to promote Al_2O_3 solid state reaction with cerium oxide. The CeO_2 - Al_2O_3 - CeAlO_3 composites have shown remarkable performances for the carbon monoxide selective oxidation showing also an acceleration of the coke oxidation.^{24,34} Other interesting structural, electric and magnetic properties have been reported for this material.^{33,35,36}

It is also worth noticing that the solubility of Al^{3+} in CGO is limited to ca. 2% molar.²⁵ Nevertheless, the solid state reaction leading to the formation of CeAlO_3 is fast and completed in the reduced form, which results in an overall composition similar to Ce_2O_3 . Accordingly, the aluminate phase can be expressed in a two-step chemical reaction:

Gas-solid reaction



Solid-solid reaction



According to thermodynamic calculation on $\text{Ce}_{0.9}\text{Gd}_{0.1}\text{O}_{1.95-\delta}$ under 9% H_2/N_2 in the temperature range of 500–1450 °C (*i.e.* $10^{-31} < p\text{O}_2 < 10^{-12}$ atm),¹⁴ CGO does not get fully reduced to the stoichiometry $\text{Ce}_{0.9}\text{Gd}_{0.1}\text{O}_{1.5}$ ($\delta = 0.45$) as in (1). However, the same calculations indicate that a stable composition of $\text{Ce}_{0.9}\text{Gd}_{0.1}\text{O}_{1.75}$ ($\delta = 0.2$) can be achieved for $T > 1100$ °C in 9% H_2/N_2 .¹⁴ Such a degree of reduction corresponds to ~45% of cerium cations with 3+ valence, *i.e.* reduction of Ce^{4+} to Ce^{3+} with release of oxygen gas (O_2), and formation of oxygen vacancies δ in the lattice, for ca. 45% of the material as in reaction (1).¹⁴ Therefore, since at $T > 1100$ °C CGO is highly diffusive (ref. 14–17 and Fig. 1 and 2), the solid-solid reaction (2) between the CGO and Al_2O_3 probably develops at the same range of temperatures over wide portions of the CGO matrix. From reaction (1) to reaction (2) cerium cations undergo several chemical expansion steps, as well as complete crystalline rearrangement. According to the solute drag theory both cations size and valences are the factors controlling the ionic diffusion and the steps (1) and (2) are related to changes in the structure. These changes are:^{35,36}

- At the step (1), from 8-fold cubic (Ce^{4+} ionic radius 0.907 Å) in CeO_2 to a 6-fold octahedral (Ce^{3+} ionic radius 1.01 Å and Gd^{3+} 1.053 Å) in Ce_2O_3 .

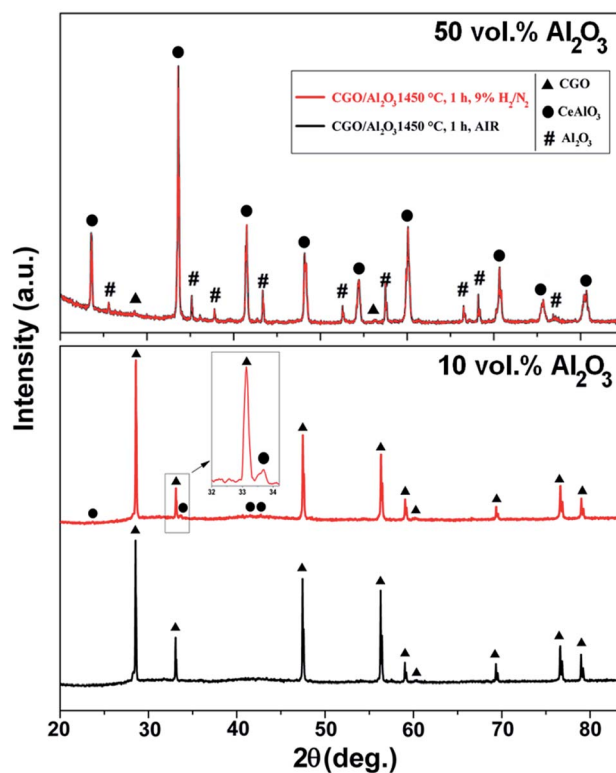


Fig. 5 XRD analysis of (bottom panel) CGO/ Al_2O_3 10 vol% Al_2O_3 sample treated in air (black pattern) and in 9% H_2/N_2 (red pattern) after sintering at 1450 °C for 1 h and (top panel) CGO/ Al_2O_3 50 vol% Al_2O_3 sample treated in 9% H_2/N_2 . Symbols indicate CGO fluorite (triangle), CeAlO_3 perovskite (circles) and α - Al_2O_3 (dash).

- At the step (2), from a 6-fold octahedral (Ce^{3+} ionic radius 1.01 Å and Gd^{3+} 1.053 Å) in Ce_2O_3 to a 12-fold cuboctahedral coordination (Ce^{3+} ionic radius 1.34 Å) in CeAlO_3 .

On the other hand Al^{3+} remains at 6-fold octahedral coordination (Al^{3+} ionic radius 0.535 Å) and both Ce and Al are eventually stabilised in the cerium-aluminate form. This study shows that, since both densification and grain growth are limited in the reacted CGO/ Al_2O_3 composite in reducing conditions, CeAlO_3 possesses limited mass diffusion. Moreover, due to the limited solubility of Al in CeO_2 , Al_2O_3 particles inhibit the densification of the CGO matrix by a possible pinning effect.

3.4. Electrochemical properties

The electrochemical properties of the composites were investigated by EIS measurements. Nyquist plots at low temperatures, as the one shown in Fig. 6a, exhibit two depressed semicircles well separated in the frequency domain. In the composite samples, the high frequency (HF) semicircle is related to the oxygen ion transport in bulk CGO (ρ_{HF}), whereas the low frequency (LF) one is associated with blocking (ρ_{LF}) of charge carriers by both grain boundaries, pores and the (insulating) alumina.²⁷ The low frequency end spike is due to Pt electrodes. Electrical resistivity components were determined by fitting EIS data to two parallel resistor/constant phase element circuits connected in series. The major contribution to the total

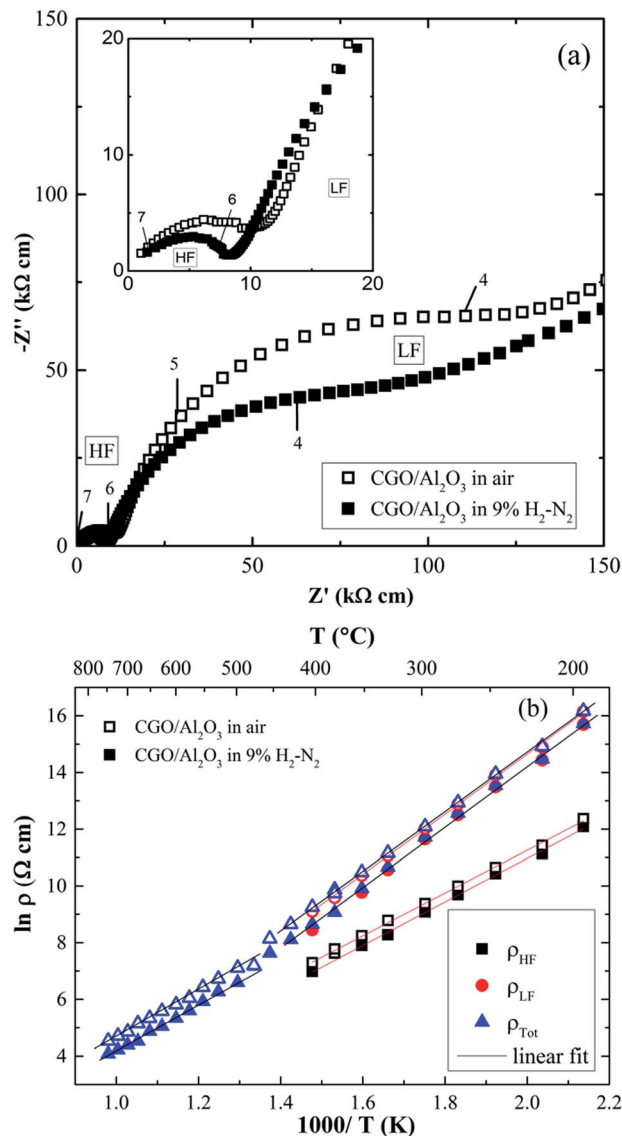


Fig. 6 (a) Nyquist plot measured at 300 °C. Numbers indicate the logarithm of frequency. (b) Arrhenius plots of the electrical resistivity components obtained from EIS analysis of CGO/Al₂O₃ samples treated in air and in 9% H₂/N₂, after sintering at 1450 °C for 1 h.

electrical resistivity ($\rho_{\text{Tot}} = \rho_{\text{HF}} + \rho_{\text{LF}}$) is the low frequency blocking resistivity as previously observed in similar composites having insulating phases in an ionic conductor matrix. Fig. 6b shows the Arrhenius plots of the electrical resistivity components ($\rho_{\text{Tot}} = \rho_{\text{HF}} + \rho_{\text{LF}}$). Samples display similar thermally activated behaviour regardless the sintering conditions, being the sample sintered in air slightly more resistive than the one sintered in 9% H₂. The Arrhenius plot exhibits the characteristic deviation previously observed for ceria-based electrolytes at $T \sim 450$ °C.^{17,28} In the low temperature region ($T < 450$ °C), calculated activation energies were: air -bulk 0.65 eV, LF 0.91 eV, total 0.90 eV; 9% H₂ -bulk 0.66 eV, LF 0.94 eV total 0.92 eV. At higher temperatures (>450 °C) only the total resistivity was analysed and corresponding activation energies were very similar for both samples (0.71 eV). Such values are comparable to

previously reported bulk activation energy for oxygen ion transport in CGO,²⁸ indicating that both CGO is the percolating phase and that electronic charge carriers were prevented by the high temperature re-oxidation step. On the other hand, the blocking resistivity displays considerable higher activation energy values. Such a feature has been observed in composites comprised of an ion conductor matrix and insulating second phase, in which the activation energy of the low frequency component is increased with respect to the one of bulk due to the blocking of charge carriers.²⁷

A more detailed analysis of the impedance data is hampered by the complex microstructural features of composite samples discussed in the previous sections. Nonetheless, to gain further insight from EIS data, Bode plots corresponding to the data in Fig. 6a, are shown in Fig. 7. The module dependence on the frequency displays similar behaviour for both samples. On the other hand, the frequency dependence of the phase shift reveals that, while HF (bulk) relaxations occur at essentially the same frequency for both samples, the low frequency component has a marked dependence on the sintering environment. The relaxation of the LF component of the sample sintered in reducing conditions is broader and it occurs at lower frequency than that of samples sintered in air. Considering that both samples have comparable LF (blocking) resistivity and the relaxation frequency is *circa* one order of magnitude lower for the sample sintered in hydrogen, there is a significant change in the LF capacitance depending on the sintering conditions. Such a difference reflects the different electrochemical properties of the low frequency component, associated with the intergranular blockers (pores, grain boundaries, and insulating phases) in the two samples. It is important to take into account that apparent densities of samples sintered in both air and reducing conditions differ only $\sim 10\%$, which is probably insufficient to account for such a significant change in the capacitance.³⁷ Therefore, it is likely that the capacitance of the sample sintered in H₂ is affected by the formation of CeAlO₃ phase. Nevertheless, it is interesting to note that the CeAlO₃ phase is associated

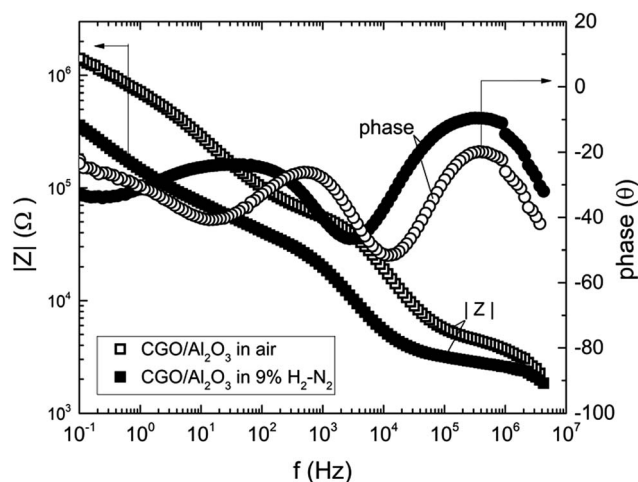


Fig. 7 Bode plots measured at 300 °C for CGO/Al₂O₃ samples treated in air and in 9% H₂/N₂ after sintering at 1450 °C for 1 h.

with intergranular porosity, as observed in Fig. 3. Thus, EIS analyses evidenced distinct electrochemical properties of samples sintered in different oxygen partial pressure, a feature mostly related to the solid state reaction between doped-ceria and alumina in reducing conditions.

4. Conclusions

Gadolinium-doped ceria presents fast mass diffusion effects at low oxygen partial pressure ($pO_2 < 10^{-12}$ atm) and relatively low temperatures (~ 800 °C). Such mass diffusion effects are activated by fast cation migration mechanisms of the highly defective CeO₂. Under reducing conditions, ceria can react with alumina at temperature about 1100 °C, resulting in an additional phase in CGO/Al₂O₃ ceramic composites. Such phase was identified as CeAlO₃ and found embedded in a complex microstructural and compositional arrangement with lamellar, porous and spherical hollow features. The CeAlO₃ is not formed in oxidative conditions due to the limited solubility of Al³⁺ in CGO. However, in reducing conditions CeAlO₃ is probably formed by a substantial reduction of CeO₂ to Ce₂O₃. During the sintering process of CGO/Al₂O₃, such a solid state reaction at low pO_2 hinders densification and grain growth. Consequently, the composite treated in reducing conditions at high temperatures (1450 °C) remains porous. At 1450 °C, the relative fraction of 10 vol% of α -Al₂O₃ used in the CGO/Al₂O₃ composites reacts almost completely. Few alumina nanoparticles left in the samples are completely surrounded by shell-like formation of the new phase, displaying complex microstructural features with lamellar formations. Composite samples sintered in air and in reducing conditions exhibit similar electrical resistivity and activation energies for both bulk and blocking of charge carriers at low frequency, confirming that CGO is the percolating phase. However, Bode plots indicated that the electrochemical properties of low frequency component are dependent on the chemical treatments. Such dependence reflects the complex microstructure of composites sintered in reducing conditions and is further evidence of the solid state reaction between Al/Ce that resulted in the formation of CeAlO₃.

Acknowledgements

VE and FCF are thankful for the partial support of the Brazilian agency CNPq (projects no. 401218/2014-7 and no. 300961/2013-8).

Notes and references

- 1 A. Trovarelli, *Catal. Rev.: Sci. Eng.*, 1996, **38**, 439.
- 2 M. Ni, D. Y. C. Leung and M. K. H. Leung, *Int. J. Hydrogen Energy*, 2007, **32**, 3238.
- 3 B. C. H. Steele, *Solid State Ionics*, 2000, **129**, 95.
- 4 C. William and S. Haile, *Philos. Trans. R. Soc., A*, 2010, **368**, 3269.
- 5 V. V. Kharton, A. V. Kovalevsky, A. P. Viskup, A. L. Shaula, F. M. Figueiredo, E. N. Naumovich and F. M. B. Marques, *Solid State Ionics*, 2003, **160**, 247.
- 6 V. V. Kharton, F. M. B. Marques and A. Atkinson, *Solid State Ionics*, 2004, **174**, 135; M. Mogensen, N. M. Sammes and G. A. Tompsett, *Solid State Ionics*, 2000, **129**, 63; M. V. Ganduglia-Pirovano, A. Hofmann and J. Sauer, *Surf. Sci. Rep.*, 2007, **62**, 219.
- 7 S. McIntosh and R. J. Gorte, *Chem. Rev.*, 2004, **104**, 4845.
- 8 H. Huang, W. Shan, S. Yang and J. Zhang, *Catal. Sci. Technol.*, 2014, **4**, 3611.
- 9 J. Y. Park, H. Yoon and E. D. Wachsman, *J. Am. Ceram. Soc.*, 2005, **88**, 2402.
- 10 S. Sanna, V. Esposito, J. W. Andreasen, J. Hjelm, W. Zhang, T. Kasama, S. B. Simonsen, M. Christensen, S. Linderroth and N. Pryds, *Nat. Mater.*, 2015, **14**, 500.
- 11 J. E. Miller, M. D. Allendorf, R. B. Diver, L. R. Evans, N. P. Siegel and J. N. Stuecker, *J. Mater. Sci.*, 2008, **43**, 4714–4728; P. Furler, J. R. Scheffe and A. Steinfeld, *Energy Environ. Sci.*, 2012, **5**, 6098; G. P. Smestad and A. Steinfeld, *Ind. Eng. Chem. Res.*, 2012, **51**, 11828.
- 12 E. V. Ramos-Fernandez, N. R. Shiju and G. Rothenberg, *RSC Adv.*, 2014, **4**, 16456.
- 13 S. Ackermann, J. R. Scheffe and A. Steinfeld, *J. Phys. Chem. C*, 2014, **118**, 5216.
- 14 V. Esposito, D. W. Ni, Z. M. He, W. Zhang, A. S. Prasad, J. A. Glasscock, C. Chatzichristodoulou, S. Ramousse and A. Kaiser, *Acta Mater.*, 2013, **61**, 6290.
- 15 F. Teocoli, D. W. Ni and V. Esposito, *Scr. Mater.*, 2015, **94**, 13.
- 16 F. Teocoli and V. Esposito, *Scr. Mater.*, 2014, **75**, 82.
- 17 D. W. Ni, J. A. Glasscock, A. Pons, W. Zhang, A. Prasad, S. Sanna, N. Pryds and V. Esposito, *J. Electrochem. Soc.*, 2014, **161**, F3072.
- 18 P.-L. Chen and I.-W. Chen, *J. Am. Ceram. Soc.*, 1994, **77**, 2289; P.-L. Chen and I.-W. Chen, *J. Am. Ceram. Soc.*, 1996, **79**, 1793.
- 19 J. A. Glasscock, V. Esposito, S. P. V. Foghmoes, T. Stegk, D. Matuschek, M. W. H. Ley and S. Ramousse, *J. Eur. Ceram. Soc.*, 2013, **33**, 1289; D. Z. de Florio, V. Esposito, E. Traversa, R. Muccillo and F. C. Fonseca, *J. Therm. Anal. Calorim.*, 2009, **97**, 143; D. W. Ni, C. G. Schmidt, F. Teocoli, A. Kaiser, K. B. Andersen, S. Ramousse and V. Esposito, *J. Eur. Ceram. Soc.*, 2013, **33**, 2529.
- 20 D. W. Ni, K. B. Andersen and V. Esposito, *J. Eur. Ceram. Soc.*, 2014, **34**, 3769.
- 21 S. Roy and A. Baiker, *Chem. Rev.*, 2009, **109**, 4054; S. Bernal, J. J. Calvino, M. A. Caqui, J. M. Gatica, C. Larese, J. A. Perez Omil and J. M. Pintado, *Catal. Today*, 1999, **50**, 175; A. Trovarelli, C. de Leitenburg, M. Boaro and G. Dolcetti, *Catal. Today*, 1999, **50**, 353.
- 22 S. Damyanova, C. A. Perez, M. Schmal and J. M. C. Bueno, *Appl. Catal., A*, 2012, **234**, 271.
- 23 T. Y. Kim, S. M. Kim, W. S. Lee and S. I. Woo, *Int. J. Hydrogen Energy*, 2013, **38**, 6027.
- 24 P. A. Deshpande, S. T. Aruna and G. Madras, *Catal. Sci. Technol.*, 2011, **1**, 1683.
- 25 J.-S. Lee, K.-H. Choi, B.-K. Ryu, B.-C. Shin and I.-S. Kim, *Ceram. Int.*, 2004, **30**, 807.
- 26 Y.-M. Chiang, D. Birnie III and W. D. Kingery, in *Physical ceramics, principles for ceramics and engineering, MIT series*

- in material science and engineering*, Wiley, New York, ch. 5, 1996.
- 27 F. C. Fonseca and R. Muccillo, *Solid State Ionics*, 2004, **166**, 157; M. Kleitz, L. Dessemond and M. C. Steil, *Solid State Ionics*, 1995, **75**, 107; F. C. Fonseca and R. Muccillo, *Solid State Ionics*, 2000, **131**, 301.
- 28 D. Z. de Florio, R. Muccillo, V. Esposito, E. Di Bartolomeo and E. Traversa, *J. Electrochem. Soc.*, 2005, **152**, A88; V. Esposito and E. Traversa, *J. Am. Ceram. Soc.*, 2008, **91**, 1037.
- 29 R. Bollina and R. M. German, *In situ* evaluation of viscosity during sintering of boron doped stainless steel using bending beam technique, in *Proceedings of World PM2004*, EPMA, Vienna, Shrewsbury, 2004; F. Teocoli, D. W. Ni, K. Brodersen, S. P. V. Foghmoes, S. Ramousse and V. Esposito, *J. Mater. Sci.*, 2014, **49**, 5324.
- 30 D. W. Ni, V. Esposito, S. P. V. Foghmoes and S. Ramousse, *J. Eur. Ceram. Soc.*, 2014, **34**, 2371.
- 31 M. Fernandez-Garcia, A. Martinez-Arias, A. B. Hungria, A. Iglesias-Juez, J. C. Conesa and J. Soria, *Phys. Chem. Chem. Phys.*, 2002, **4**, 2473.
- 32 S. T. Aruna, N. S. Kini, S. Shettyb and K. S. Rajama, *Mater. Chem. Phys.*, 2010, **119**, 485 A. S. Prakash, C. Shivakumara and M. S. Hegde, *Mater. Sci. Eng., B*, 2007, **B13**, 55.
- 33 Y. S. Kim, *Acta Crystallogr.*, 1968, **B24**, 295; T. Shishido, H. Iwasaki and N. Toyota, *J. Alloys Compd.*, 1994, **209**, L11; L. Vasylechko, A. Senyshyn, D. Trots, R. Niewa, W. Schnelle and M. Knapp, *J. Solid State Chem.*, 2007, **180**, 1277.
- 34 A. Piras, A. Trovarelli and G. Dolcetti, *Appl. Catal., B*, 2000, **28**, L77.
- 35 M. Tanaka, T. Shishido, H. Horiuchi, N. Toyota, D. Shindo and T. Fukuda, *J. Alloys Compd.*, 1993, **192**, 87.
- 36 T. Shishido, H. Iwasaki, N. Toyota, M. Tanaka, H. Horiuchi, S. Nojima, S. Nakagawa and T. Fukuda, *J. Alloys Compd.*, 1994, **209**, L11.
- 37 M. C. Steil, F. Thevenot and M. Kleitz, *J. Electrochem. Soc.*, 1997, **144**, 390.